Near-wall treatment for the simulation of turbulent flow by the cumulant lattice Boltzmann method

Andrea Pasquali, Martin Geier*, Manfred Krafczyk

Institut für Rechnergestützte Modellierung im Bauingenieurwesen (iRMB)
Technische Universität Braunschweig
Pockelsstr. 3, 38106 Braunschweig, Germany

November 5, 2017

Abstract

We present a new wall function implementation for the cumulant lattice Boltzmann method that sets a partial slip velocity on the wall by computing a skin frictional coefficient. Our approach uses local information and is particularly appropriate for implementations on general purpose graphics processing units. The validation of the model has been conducted by performing numerical simulations of the turbulent channel flow test case with different grid resolutions and for different Reynolds numbers. The results showed encouraging agreement with Direct Numerical Simulation data for both velocity profile and Reynolds shear stresses.

Keywords

Turbulence, Wall function, Partial slip velocity boundary condition, cumulant lattice Boltzmann method, General-purpose graphics processing units

*Corresponding author: geier@irmb.tu-bs.de

1 Introduction

Near-wall turbulence is one of the most interesting subjects of turbulence itself because it is responsible for some important effects such as friction drag and wall heat transfer. Turbulent flows can be characterized as inherently unsteady, irregular and three-dimensional making the study of such flows difficult. However, the velocity profile in the near-wall region often has a particular well-defined shape, which can be described with the "law of the wall" [1]. Experimental measurements and Direct Numerical Simulation (DNS) results of a flow confined between two parallel planes confirm this velocity profile [2]. For flows at high Reynolds numbers, the near-wall region (or boundary layer) is a region of strong velocity gradients because the velocity is zero exactly at the wall and approaches the bulk velocity over a short distance. Due to these strong gradients present in the proximity of the wall, in Computational Fluid Dynamics (CFD) highly refined grids are required in order to resolve the boundary layer.

In order to predict the correct velocity profile and stresses at the wall, the study of near-wall region flows has initiated the development of appropriate mathematical models, the so-called "wall functions". The use of wall functions avoids the explicit spatio-temporal discretization of the viscous sub-layer and thus drastically decreases the computational effort. The first wall function was introduced by Launder and Spalding in 1974 [3]. The idea is to use the law of the wall to compute the wall shear stress τ_w and to adjust the eddy viscosity for the first grid node accordingly to τ_w. Thus, a wall function simulation normally requires that the first cell outside the walls lies in the logarithmic region ($y^+ > 30$). Other wall functions have been implemented to work properly with smaller y^+ [4, 5], and to take the pressure gradients into account [6, 7], which can occur when the flow separates from the surface, e.g. with curved geometries [8]. It is worth mentioning that each wall function implementation is strictly related to the turbulence model used. For this reason, the implementation of a specific wall function for a different simulation approach is not straightforward. A more general implementation is the use of a skin friction boundary condition as wall function [9, 10]. The latter sets a partial slip velocity on the surface of the wall and it is not related to the specific simulation approach used.

The lattice Boltzmann method (LBM) has been widely used in CFD for simulations of incompressible flows including turbulent channel flows with resolved boundary layers [11, 12] using surface refined grids [13]. However, it has only recently been used for the implementation of a near-wall region treatment [14, 15]. The implementation of [15] reconstructs the distributions of the first grid point by evaluating a deviatoric stress. It considers the fluid density and velocity at the second node from the wall in the normal direction, and recomputes their values at the boundary node.

In this work we present a new wall function for the LBM which uses only information at the boundary nodes (first grid node). After recomputing the quantities at the wall, the wall function imposes a partial slip velocity at the boundary surface in order to satisfy the skin friction requirement. The use of the boundary node for the evaluation of the wall function facilitates the implementation of our model, especially for implementations on general purpose graphics processing units (GPGPU) where the locality of the information is essential for efficiency of the GPGPU.

The paper continues with an introduction to boundary layer theory (Sec. 2), the cumulant LBM and the computation of required quantities at the wall (Sec. 3), and the implementation of the wall function (Sec. 4). Finally, we show numerical results for the turbulent channel flow simulation with different grid resolutions and at different Reynolds numbers (Sec. 5), and discuss our approach in the conclusion (Sec. 6).

2 Thin boundary layer approximation

The Navier-Stokes (NS) equations accurately describe the mechanics of viscous fluids on macroscopic scales by a momentum transport equation:

$$\partial_t \vec{u} + (\vec{u} \cdot \nabla)\vec{u} = -\frac{1}{\rho}\nabla p + \nu \nabla^2 \vec{u} + \vec{g}, \tag{1}$$

and a continuity equation:

$$\nabla \cdot \vec{u} = 0. \tag{2}$$

Eq. (1) and Eq. (2) are written in incompressible form where $\vec{u} = (u, v, w)$ is the velocity of the flow field, ρ is the density, p is the pressure, ν is the kinematic viscosity, and $\vec{g} = (g_x, g_y, g_z)$ is an acceleration due to a body force. By assuming the thin layer approximation [16–18] we can simplify this set of equations in order to solve them for the near-wall region. The hypotheses are: i) neglect of diffusion processes parallel to a body surface, ii) replacement of the momentum equation normal to the surface with the assumption of zero normal pressure gradient throughout the boundary layer. This means that we assume the mean flow as parallel to the wall and statistically steady. Considering, for example, a flat wall with a fluid flow moving in X-direction with the normal to the wall in Y-direction, we have that:

$$v \ll u, \quad \partial_x u \ll \partial_y u, \quad \partial_t u = 0, \quad \partial_y p = 0, \tag{3}$$

and Eq. (1) for the X-direction component reduces to:

$$0 = -\partial_x p + \partial_y(\mu \partial_y u) + \rho g_x, \tag{4}$$

where $\mu = \rho\nu$ is the dynamic viscosity and the term $-\partial_x p$ is the pressure gradient in the direction parallel to the wall. Eq. (4) is solved to obtain the wall shear stress τ_w:

$$\tau_w = \mu \partial_y u, \tag{5}$$

and the frictional velocity u_τ:

$$u_\tau = \sqrt{\tau_w/\rho}. \tag{6}$$

In order to express the turbulent boundary layer quantities in dimensionless form, it is possible to define the dimensionless wall distance y^+:

$$y^+ = \frac{y}{\nu} u_\tau, \tag{7}$$

and the dimensionless velocity u^+:

$$u^+ = \frac{u}{u_\tau}. \tag{8}$$

Another important quantity is the skin-friction coefficient C_f:

$$C_f = \frac{\tau_w}{1/2 \rho u_\infty^2}, \tag{9}$$

with u_∞ the free-stream velocity.

A standard approach to solve Eq. (4) is to integrate in the direction normal to the wall and solve for the first derivative of the velocity with a Gauss-Legendre quadrature method [19]. The method has to be supplemented by a Newton algorithm for obtaining τ_w. By using the cumulant LBM, in the case of flat walls, it is possible to have directly the second derivative of the velocity.

3 Cumulant LBM

The LBM is a numerical method for solving the weakly compressible NS equations. It is motivated by the Boltzmann transport equation and deals with a discrete local distribution function in momentum space, f [20]. The discrete lattice Boltzmann equation in three dimensions is written as:

$$f_{ijk(x+ic\Delta t)(y+jc\Delta t)(z+kc\Delta t)(t+\Delta t)} = f_{ijkxyzt} + \Omega_{ijkxyzt} = f^*_{ijkxyzt}, \tag{10}$$

where ic, jc, and kc are the components in velocity space, $c = {}^{\Delta x}/_{\Delta t}$ is the discrete speed and i, j, $k \in \mathbb{Z}$ and x, y, and z are the variables in space, t is the time variable, Ω is the collision operator, and the symbol $*$ means the post-collision state. The evolution of the flow field is split into two steps: the streaming step propagates the distributions according to their respective momentum direction from node to node (LHS of Eq. (10)) and the collision step rearranges the local distributions on each node (RHS of Eq. (10)). The accuracy of the results and the stability of the method depend on the collision operator Ω.

The cumulant LBM is a multiple relaxation time LBM that uses cumulants as quantities for the collision operation [21]. Cumulants are the variables of the continuous particle distribution function after Laplace-transforming the discrete f from time-velocity-space to frequency-velocity-space:

$$C_{\alpha\beta\gamma} = c^{-\alpha-\beta-\gamma} \frac{\partial^\alpha \partial^\beta \partial^\gamma}{\partial \Xi^\alpha \partial \Upsilon^\beta \partial Z^\gamma} \ln(\mathcal{L}\{f_{ijk}(ic, jc, kc)\})\Big|_{\Xi=\Upsilon=Z=0}, \tag{11}$$

where Ξ, Υ and Z are the coordinates of the frequency-velocity-space. Cumulants are thus observable quantities, which are both Galilean invariant and statistically independent of each other. They are used only in the collision step where each cumulant is relaxed towards its equilibrium with an individual rate $\omega_{\alpha\beta\gamma}$:

$$C^*_{\alpha\beta\gamma} = \omega_{\alpha\beta\gamma} C^{eq}_{\alpha\beta\gamma} + (1 - \omega_{\alpha\beta\gamma}) C_{\alpha\beta\gamma}, \tag{12}$$

where $C^*_{\alpha\beta\gamma}$ and $C^{eq}_{\alpha\beta\gamma}$ indicate the post-collision and the equilibrium state of the cumulants, respectively. After collision, the post-collision particle distribution function f^* is obtained by a backward transformation from $C^*_{\alpha\beta\gamma}$ [21].

3.1 Second derivative of the velocity by using cumulants

After performing asymptotic analysis of Eq. (10) up to third order in diffusive scaling, the relationship between the third order cumulants and the second derivative of the velocity is found [22]:

$$\frac{C^*_{120} - C_{120} - {}^1\!/_3 \rho g_x}{-\frac{2}{9}\rho\left(\frac{1}{\omega_1} - \frac{1}{2}\right)} = 2\partial_{xy} v + \partial_{yy} u + \mathcal{O}(\Delta x^2), \tag{13}$$

where ω_1 is the relaxation rate related to the kinematic viscosity:

$$\nu = \frac{1}{3}\left(\frac{1}{\omega_1} - \frac{1}{2}\right), \tag{14}$$

and C^*_{120} and C_{120} are the third order cumulants in xyy for the post-collision and pre-collision states, respectively. By considering the thin boundary layer approximation ($v \ll u$), the mixed derivative $\partial_{xy} v$ can be neglected:

$$\partial_{yy} u \approx \frac{C^*_{120} - C_{120} - {}^1\!/_3 \rho g_x}{-\frac{2}{9}\rho\left(\frac{1}{\omega_1} - \frac{1}{2}\right)}. \tag{15}$$

This allows to solve directly the second derivative of the velocity of Eq. (4) and to obtain the wall shear stress τ_w. For the first fluid node close to the wall it is possible to write:

$$\partial_y(\mu \partial_y u) = \partial_y(\tau_w) \approx \Delta\tau_w / \Delta y, \tag{16}$$

$$\mu \partial_{yy} u = \frac{\tau_{xy} - \tau_w}{y_w}, \tag{17}$$

$$\tau_w = \tau_{xy} - y_w \mu \partial_{yy} u, \tag{18}$$

where y_w is the distance to the wall, and the deviatoric stress tensor component τ_{xy} is locally evaluated at the first fluid node close to the wall by using cumulants:

$$-C_{110}\frac{3\omega_1}{\rho} = \partial_x v + \partial_y u + \mathcal{O}(\Delta x^2), \tag{19}$$

$$\tau_{xy} \approx \mu\left(-C_{110}\frac{3\omega_1}{\rho}\right), \tag{20}$$

where C_{110} is the second order cumulant in xy.

The derivation of Eq. (15) is given in Appendix A. In contrast to the cumulant method it is not straightforward to extract second derivatives of velocities from a moment based or BGK Lattice Boltzmann method. Moments by itself have no direct relationship to the second order derivatives. Still it would be possible to compute cumulants for a moment based collision operator. However, moment based collision operators are usually not second order accurate for third order moments or cumulants. This arises form (among other defects) the neglect of third order terms in the Mach number expansion of the equilibrium on which the standard MRT methods are based [23]. The information on second derivatives of velocities, which we are able to extract from the cumulant method due to its superior accuracy, is found at the third asymptotic order in diffusive scaling of the third cumulants which is beyond the cut-off accuracy of the Taylor expanded equilibrium used in most lattice Boltzmann schemes.

3.2 Relaxation rates for the third order cumulants

The third order cumulants used for deriving the second derivative of the velocity and thus τ_w are relaxed towards their equilibrium by the specific relaxation rates ω_3, ω_4, and ω_5 [21]:

$$C^*_{120} + C^*_{102} = (1 - \omega_3)(C_{120} + C_{102}), \tag{21}$$

$$C^*_{210} + C^*_{012} = (1 - \omega_3)(C_{210} + C_{012}), \tag{22}$$

$$C^*_{201} + C^*_{021} = (1 - \omega_3)(C_{201} + C_{021}), \tag{23}$$

$$C^*_{120} - C^*_{102} = (1 - \omega_4)(C_{120} - C_{102}), \tag{24}$$

$$C^*_{210} - C^*_{012} = (1 - \omega_4)(C_{210} - C_{012}), \tag{25}$$

$$C^*_{201} - C^*_{021} = (1 - \omega_4)(C_{201} - C_{021}), \tag{26}$$

$$C^*_{111} = (1 - \omega_5)C_{111}. \tag{27}$$

Previous works showed that with an appropriate combination of the odd and even rates it was possible to improve the accuracy of the results for bounded flows (Ginzburg parameters) [24, 25]. In this work we used a combination of the relaxation rates that reduces the numerical dissipation [22, 26]. In terms of Ginzburg parameters, the coefficients are:

$$\Lambda_3 = 1/12, \quad \Lambda_4 = 1/6, \quad \Lambda_5 = 7/24, \tag{28}$$

and the new relaxation rates written as function of ω_1 are:

$$\omega_3 = \frac{3(\omega_1 - 2)}{\omega_1 - 3}, \quad \omega_4 = \frac{6(\omega_1 - 2)}{\omega_1 - 6}, \quad \omega_5 = \frac{12(2 - \omega_1)}{12 + \omega_1}. \tag{29}$$

We note here that while these parameters reduce dissipation compared to $\omega_3 = \omega_4 = \omega_5 = 1$ they do not increase the convergence order of the method. After the current paper was submitted a better parametrization has been found that also improves the convergence order of the viscous term [27]. This new parametrization was shown to work in combination with very large Reynolds numbers and the drag crisis behind a sphere could be captured [28].

Reducing the numerical dissipation leads to a more realistic turbulence intensity. However, it also reduces the stability of the simulation at high Reynolds number (and with under-resolved grids). In order to have accurate and stable simulations, we applied a limiter coefficient $c_{lim} \in \mathbb{R}^+$ for the relaxation rates [22]. The new relaxation rates with the limiter coefficient are shown in Appendix B. In Appendix C we show the comparison of the new relaxation rates with the standard set equal to unity ($\omega_3 = \omega_4 = \omega_5 = 1$) for the same test case used for the validation of the wall function.

4 Frictional partial slip velocity wall function

The frictional partial slip velocity wall function (FPSV-WF) is based on five inputs. These are the fluid velocity $\vec{u}$, the deviatoric stress tensor $\boldsymbol{\tau}$, the second derivative of the wall tangential velocity $\partial_{nn} u_e$, the normal to the wall $\vec{n}$, and the distance to the wall y_w. The wall tangential velocity is defined as $u_e = |\vec{u} - \vec{n}(\vec{n} \cdot \vec{u})|$. The input quantities $\vec{u}$, $\boldsymbol{\tau}$, and $\partial_{nn} u_e$ are related to the evolution of the flow and they are computed and updated by the LBM kernel, while $\vec{n}$ and y_w are geometrical information provided by the grid generator `LBMHexMesh` [22, 29] and they are constant during the simulation for the flow problems investigated in this paper. All the inputs are localized on the first fluid node next to the wall.

The configuration of the boundary node is shown in Figure 1. The first fluid node next to the wall is the boundary node and it owns the information from the mesh generation, $\vec{n}$ and y_w. The LBM kernel computes the standard streaming and collision operations for all the nodes of the domain, and $\vec{u}$, $\boldsymbol{\tau}$, and $\partial_{nn} u_e$ can be computed from the cumulants. The boundary condition kernel for the wall function uses this information for imposing a slip velocity at the wall.

The FPSV-WF acts in five steps (Figure 2). The first step computes the streamwise direction $\vec{e}$ at the first fluid node with:

$$\vec{e} = \frac{\vec{u} - (\vec{u} \cdot \vec{n})\vec{n}}{\|\vec{u} - (\vec{u} \cdot \vec{n})\vec{n}\|}. \tag{30}$$

The second step calculates the wall shear stress τ_w. Two methods for computing τ_w are implemented, either by solving the second derivative of the velocity for flat walls with cumulants (D2V) or by solving the quasi-analytical solution from Musker [4]. D2V is solved by using Eq. (18). To compute the quasi-analytical solution it is necessary to calculate the stream-wise velocity $u_e = \vec{u} \cdot \vec{e}$ and to solve the Musker law by using a Newton algorithm. After obtaining τ_w, with both methods the frictional velocity u_τ is computed with Eq. (6).

Once u_τ is obtained, the skin-friction coefficient C_f can be calculated (third step). By

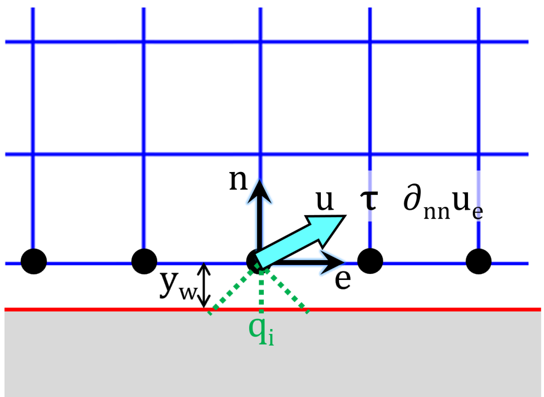

Figure 1: The information necessary for the FPSV-WF is local and stored at the first fluid node close to the wall. The sub-grid-distance q is used for the interpolated bounce-back operation.

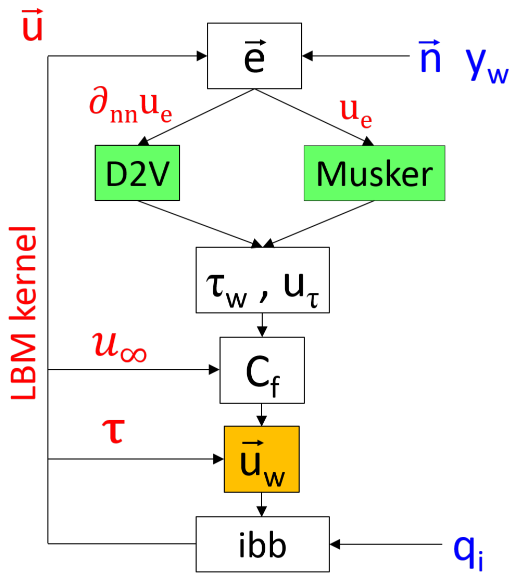

Figure 2: Functional flow block diagram of the FPSV-WF.

substituting Eq. (6) into Eq. (9), it is possible to write:

$$C_f = 2\frac{u_\tau^2}{u_\infty^2}. \tag{31}$$

For simulations where a force term is used, the free-stream velocity u_∞ is evaluated as the mean velocity in the bulk $\langle u_b \rangle$. The symbol $\langle \cdot \rangle$ indicates the average in space. When setting an inlet boundary condition where the velocity is known, the reference velocity can be used for u_∞.

With the skin-friction coefficient a partial slip velocity can be imposed at the wall $\vec{u}_w$ [9] (fourth step):

$$\vec{u}_w = -\frac{1}{C_f}\vec{n}^T \cdot \boldsymbol{\tau} \cdot \vec{e}, \tag{32}$$

where $\vec{n}^T$ is the transpose vector of $\vec{n}$. the deviatoric stress tensor $\boldsymbol{\tau}$ is locally evaluated at the boundary fluid node by using cumulants, e.g. Eqs. (19) and (20) for τ_{xy} (for the other tensor components the equations are similar by exchanging the indices).

The slip length s can be defined as [30]:

$$s = -\frac{\mu}{C_f}. \tag{33}$$

Finally, with $\vec{u}_w$ the wall function performs the fifth step, that is the interpolated bounce-back (ibb) taking into account the sub-grid-distance q [21]. More specifically we compute the pre-collision distribution comming into the fluid domain from the boundary at the next time step $f_{\bar{i}\bar{j}\bar{k}}(t + \Delta t)$ from the distributions at the same node from the previous time step as stated in [31]:

$$f_{ijk}(t + \Delta t) = \frac{1}{1+q}\left[q\left(f^*_{ijk}(t) + f^*_{\bar{i}\bar{j}\bar{k}}(t)\right) + (1-q)f_{ijk}(x)\right] - \frac{6\mathrm{w}_{ijk}(iu_w + jv_w + kw_w)}{q+1}. \tag{34}$$

In this w_{ijk} denote the lattice weights as given in [21]. The overbar on the indices indicates the inverse direction to direction ijk of the particle leaving towards the wall. The velocity components u_w, v_w and w_w denote the slip velocities at the wall which are to be calculated by the wall model. All distributions are evaluated at the same node. The boundary condition can be modified to either use only the pre- or the post-collision distributions. Using only the precollision distributions is trivially accomplished by applying the collision operator during the evaluation of the boundary condition. Using only the post-collision distributions can be accomplished by inverse BGK approximation [21]:

$$f_{ijk}(t) \approx \frac{f^*_{ijk}(t) - f^*_{ijk}(t)}{2} + \frac{f^*_{ijk}(t) + f^*_{\bar{i}\bar{j}\bar{k}}(t) - \omega_1(f^{eq}_{ijk} + f^{eq}_{\bar{i}\bar{j}\bar{k}})}{2 - 2\omega_1}. \tag{35}$$

Where f^{eq}_{ijk} is the usual BGK equilibrium distribution [21]. Note that, given a known slip velocity, this boundary condition is entirely local both in space and time.

The use of the first grid node for the evaluation of the wall model has been argued as not optimal [32]. For under-resolved grids, the information fed into the wall function at the first grid node is unavoidably affected by numerical errors, thus reducing the accuracy of the wall model [32]. Grid converged results showed better accuracy for wall function evaluations from the fourth grid node in the direction normal to the wall [32]. However, as already addressed in Sec. 1, the use of the first grid node has the advantage of not requiring any interpolation, which makes the implementation straightforward.

By considering the new relaxation rates introduced in Sec. 3.2 we reduce the numerical dissipation, thus improving the accuracy of the results. A comparison of the results obtained by the new relaxation rates with those ones obtained by the standard relaxation rates (equal to unity) is given in Appendix C.

5 Results

The FPSV-WF was validated by conducting numerical simulations of the turbulent channel flow test case for different Reynolds numbers, grid resolutions, and different methods for computing τ_w.

5.1 Computational domain and settings

The geometry of the test case is shown in Figure 3. The flow is confined between two infinite planes, one on the bottom and one on the top. All other faces represent periodic boundary conditions. The directions were stream-wise (X), normal (Y), and span-wise (Z). The height of the channel was $H = 2N$ with $N = 1\ m$ being the half channel height. In order to let the turbulence develop in both stream-wise and span-wise directions, the length L and the width W of the channel were set three times the height H ($L = W = 3H$) [15]. Uniform grids were generated by discretizing the half channel height N with three different resolutions: a very coarse one with 10 points, a less coarse one with 20 points, and

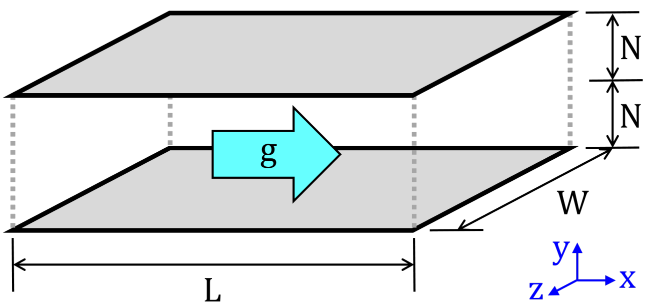

Figure 3: Channel flow between two infinite planes, at the bottom and at the top. All the other sides are periodic boundary conditions. The height of the channel is $H = 2N$, with $N = 1\ m$. The length and width are $L = W = 3H$ and the flow is driven by an acceleration $\vec{g}$.

grid name	L	W	N	H *[# points]*	Δx *[m]*	Δt *[s]*
$N10$	60	60	10	20	0.1	0.008
$N20$	120	120	20	40	0.05	0.002
$N40$	240	240	40	80	0.025	0.0005

Table 1: Summary of the grid information for the turbulent channel flow simulations.

third one with 40 points. Since the LBM computes on grids with cell aspect ratio equal to one, the discretization in the other two directions (L and W) was of the same resolution. Table 1 shows the number of points used for the three different meshes. Importantly, the choice of such coarse grids was intentional in order to stress the FPSV-WF with an under-resolved near-wall region mesh.

The flow moved inside the channel in the stream-wise direction (X) driven by an acceleration $\vec{g}$. The acceleration $\vec{g}$ was set adaptively in order to have a specific space-average velocity in the bulk domain $\vec{u}_{b,0}$ [33]:

$$\vec{g} = \left(\frac{\langle u_\tau \rangle^2}{N} + \frac{(u_{b,0} - \langle u_b \rangle) u_{b,0}}{N}, 0, 0 \right), \tag{36}$$

where $\langle u_\tau \rangle$ is the average of the computed u_τ over all the boundary nodes, and $\langle u_b \rangle$ the average over all the nodes in the bulk. The specific velocity $\vec{u}_{b,0} = (\nu Re/H, 0, 0)$ was calculated according to the simulated Reynolds number $Re = u_{b,0} H/\nu$. The Re was computed from the frictional Reynolds number $Re_\tau = u_\tau N/\nu$ by using the Dean correlation [15]:

$$Re = \left(\frac{8}{0.073} \right)^{4/7} Re_\tau^{8/7}. \tag{37}$$

In order to compare the numerical results with the DNS data, two Re_τ were chosen for which spectral method DNS experiments were available [2]. These were chosen as $Re_\tau = 950$ and $2\,000$ and they corresponded to $Re = 37\,042$ and $86\,734$, respectively. The kinematic viscosity ν and the frictional velocity u_τ were accessible from experiments [2]. In order to validate the FPSV-WF boundary condition with a higher Re, a third simulation for $Re_\tau = 16\,000$ was conducted. The specific space-average velocity $u_{b,0}$ was

Re_τ	Re	ν $[m^2/s]$ $\times 10^{-5}$	u_τ $[m/s]$	$\vec{u}_{b,0}$ $[m/s]$	$\vec{u}_{b,0,lb}$	Ma_{lb}
950	37 042	4.85909	0.04539	(0.9, 0, 0)	(0.072, 0, 0)	0.125
2 000	86 734	2.06186	0.04130	(0.9, 0, 0)	(0.036, 0, 0)	0.062
16 000	933 877	0.19277	0.03084	(0.9, 0, 0)	(0.018, 0, 0)	0.031

Table 2: Summary of the computational set-up for the turbulent channel flow simulations.

chosen equal to the previous two cases, and Re was adjusted by setting ν accordingly. All the fluid properties of the three different Re_τ are given in Table 2, together with $u_{b,0}$ and Mach number (Ma) in lattice units (subscript lb).

All the simulations were ran with the D3Q27 cumulant LBM solver `LBMCumulantFoam` [22] as under-resolved DNS without any explicit turbulence models. For the coarser grid $N10$, the time-step was $\Delta t_{N10} = 0.008$ s in order to have the maximum velocity in the bulk smaller than 0.1 in lattice units. For the other grids, the time-step was set by diffusive scaling of Δt_{N10} with respect to the cell size Δx ($\Delta t \propto \Delta x^2$). The values of the grid spacing Δx and time-step Δt for the three grids are shown in Table 1. The simulations were allowed to run over several channel passages before the analysis started. Data were obtained for the average of 60 channel passages, for a sample of nodes covering a line located at the middle of the channel from the bottom plane to the top plane. For averaging the channel was mirrored at the middle plane.

The cases for the two grid resolutions $N10$ and $N20$ and the three frictional Reynolds numbers (950, 2 000, and 16 000) were simulated with the Musker law FPSV-WF and the D2V FPSV-WF. The grid $N40$ was also simulated for the three frictional Reynolds numbers but only with the D2V FPSV-WF.

5.2 Normalized velocity profiles

The instantaneous velocity colour plot for the grid $N20$ for the three different Reynolds numbers is shown in Figure 4. The eddy sizes were largest for the lowest $Re_\tau = 950$ decreasing with higher Re (Figures 4a, 4c, and 4e). For the higher $Re_\tau = 16\,000$ the surface close to the top wall showed only few spots of low velocities (Figure 4f), resulting in a thinner boundary layer thickness. With lower Reynolds numbers the zones of small

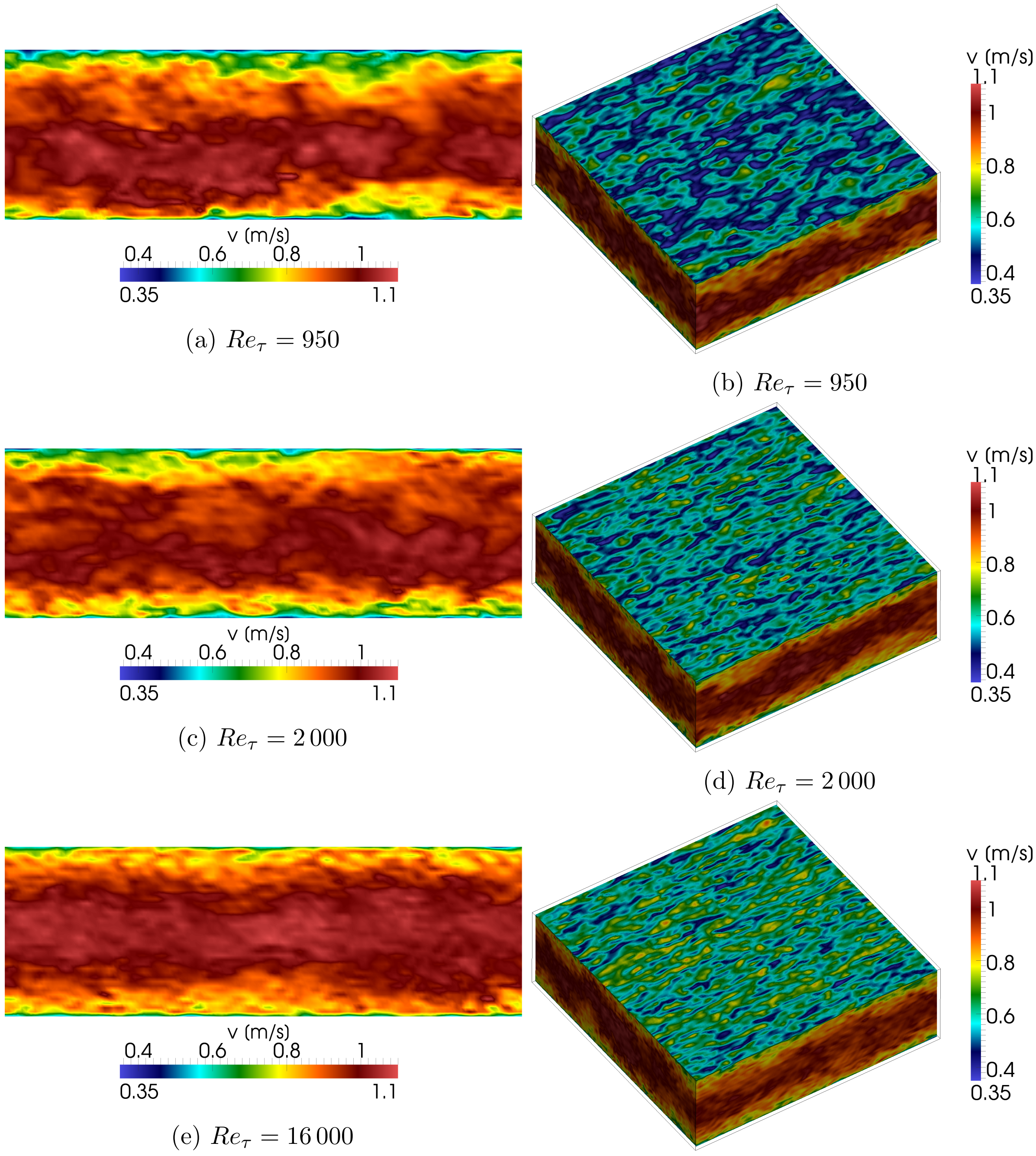

(a) $Re_\tau = 950$

(b) $Re_\tau = 950$

(c) $Re_\tau = 2\,000$

(d) $Re_\tau = 2\,000$

(e) $Re_\tau = 16\,000$

(f) $Re_\tau = 16\,000$

Figure 4: Instantaneous velocity colour plot in the channel domain for the grid $N20$ at different Re_τ by using the Musker law FPSV-WF. Slice at the centre of the channel (a, c, e) and isometric view (b, d, f).

velocities became larger, and therefore the boundary layer thickness was bigger (Figures 4d and 4b).

In order to have quantitative results for the velocity field, the normalized velocity profiles for all the simulations were measured (Figure 5). The numerical results were

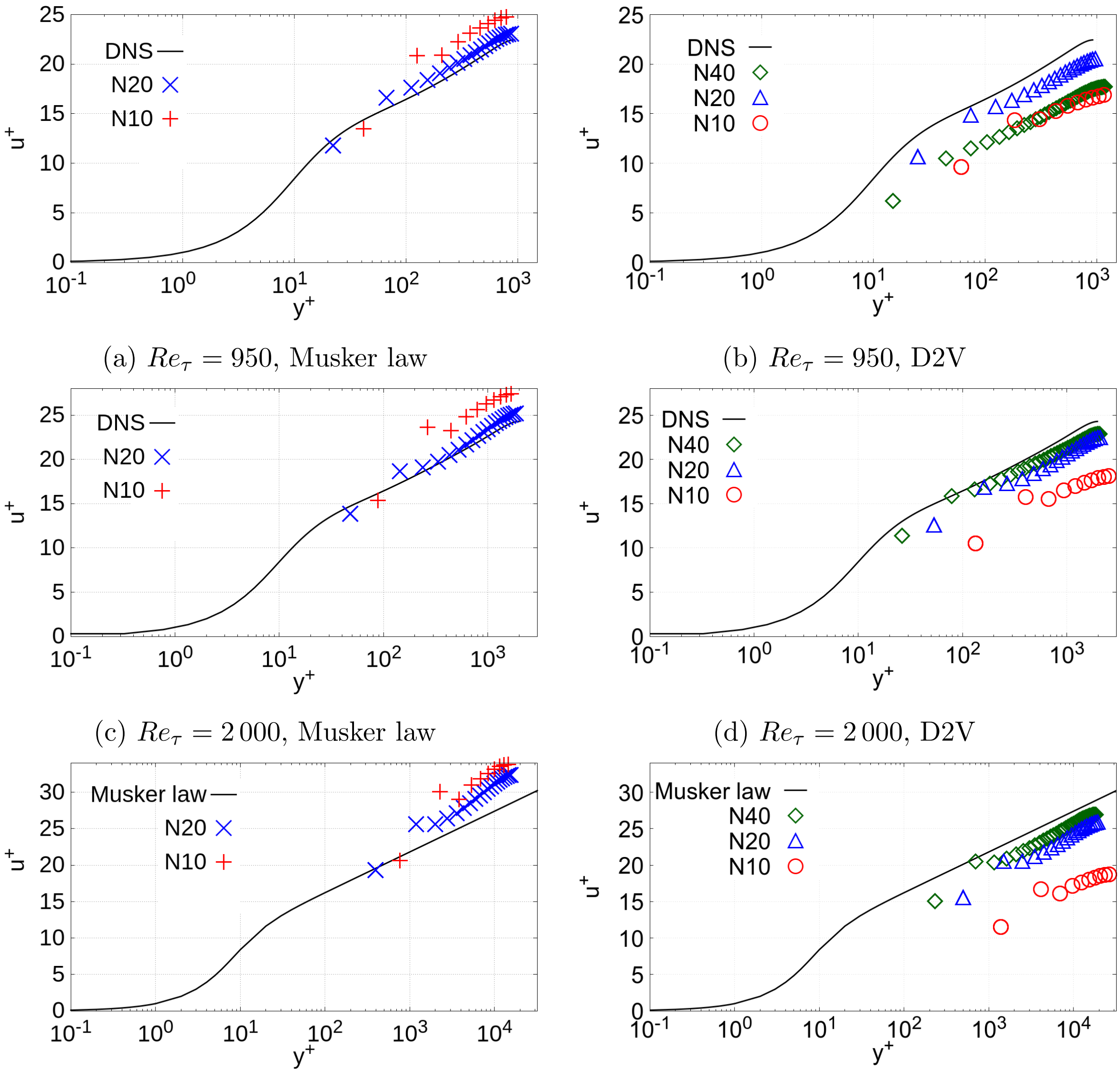

(a) $Re_\tau = 950$, Musker law

(b) $Re_\tau = 950$, D2V

(c) $Re_\tau = 2\,000$, Musker law

(d) $Re_\tau = 2\,000$, D2V

(e) $Re_\tau = 16\,000$, Musker law

(f) $Re_\tau = 16\,000$, D2V

Figure 5: Normalized velocity profile for the three different grid resolutions N10, N20, N40, the three different frictional Reynolds numbers $Re_\tau = 950$ (a, b), $Re_\tau = 2\,000$ (c, d), $Re_\tau = 16\,000$ (e, f), and the two different FPSV-WF methods, Musker law (a, c, e) and D2V (b, d, f).

compared to the DNS data [2] for the first two frictional Reynolds numbers $Re_\tau = 950$ and $2\,000$, while for the higher $Re_\tau = 16\,000$ the Musker law was used as reference.

The Musker law FPSV-WF showed reasonable results for all the Reynolds numbers and grid resolutions. Interestingly, the first point of the profile agreed well with the DNS data independently on the grid size (Figures 5a, 5c, and 5e). The rest of the profiles for the grid $N20$ was closer to the reference than for the coarser grid $N10$, thus showing a certain grid convergence of the results. Moreover, the grid $N10$ showed an evident kink at the second grid point while for the grid $N20$ this kink was smaller.

The D2V FPSV-WF showed larger discrepancies in the velocity profiles (Figures 5b, 5d, and 5f). With the very coarse mesh $N10$ the wall function overestimated the wall shear stress τ_w and consequently u_τ for all the Reynolds numbers, and the velocities were lower than in the DNS data. By increasing the resolution with the grid $N20$, the velocity profiles for the $Re_\tau = 950$ and $2\,000$ had a reasonable agreement with the DNS data, while for the higher $Re_\tau = 16\,000$ the velocities were lower. With the grid $N40$, the velocity profiles for the $Re_\tau = 2\,000$ and $16\,000$ had a better agreement with the DNS data than the grid $N20$, while for the lower $Re_\tau = 950$ this was not the case.

The deviation from the Musker law and its improvement for higher resolution is shown in Figure 6. In general, the trend is close to second order for the D2V approach except for the highest resolution and the lowest Reynolds number. In that case the y^+ of the first grid point is very close to the value of the intersection between the linear and the logarithmic profile of the "law of the wall" ($y^+ \approx 11$). This region is the zone where the transition from laminar to turbulent flow happens, which is a phenomenon very difficult to model.

Note that a wall function is, in general, applicable only if the first grid point is sufficiently far away from the wall (outer layer, $y^+ \approx 30$). However, with under-resolved grids ($y^+ > 30$) the information extracted from the first grid node necessary for applying the wall function presents errors (from the bulk), reducing the efficiency of the model

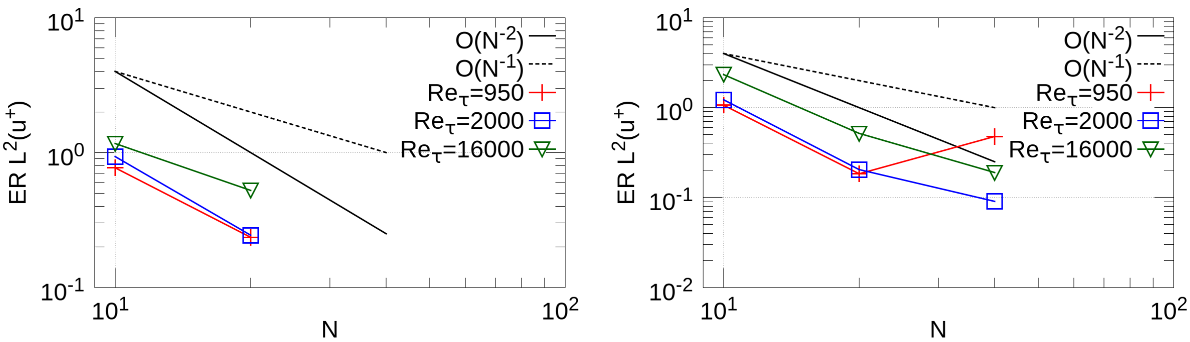

(a) Musker law (b) D2V

Figure 6: Deviation of the normalized velocity from the Musker law in the L^2-norm for the two methods and different resolution.

[32].

The grid resolutions that we used in this work, especially the very coarse one, are purely academic and can not be used for solving complex engineering cases. For giving an example, a generic car driving in a free-stream flow has $Re \approx 8\,000\,000$ (with velocity 39 m/s and reference length 3 m). By using the resolutions $\Delta x = 0.1,\ 0.05,\ 0.025\ m$ we would have $y^+ \approx 510,\ 360,\ 250$, respectively. These values of y^+ are too high for obtaining proper results from the wall model, being the information from the outer layer affected with errors. In order to apply properly the wall function for the car given in the example, we should provide $y^+ \approx 30$, which corresponds to a grid resolution of ca. $\Delta x = 0.0004\ m$.

5.3 Normalized Reynolds shear and normal stresses

The normalized Reynolds shear stress $u'v'^+$ was computed as the product of the fluctuating parts of the velocity field in the stream-wise and normal directions:

$$u'v'^+ = uv^+ - \bar{u}^+\bar{v}^+, \tag{38}$$

$$uv^+ = \frac{1}{n_t}\sum_{t=t_s}^{t_e}\frac{uv}{u_\tau^2}, \quad \bar{u}^+ = \frac{1}{n_t}\sum_{t=t_s}^{t_e}\frac{u}{u_\tau}, \quad \bar{v}^+ = \frac{1}{n_t}\sum_{t=t_s}^{t_e}\frac{v}{u_\tau}, \tag{39}$$

where t_s and t_e were the initial and final averaging time-steps, respectively, and n_t was the total number of time-steps used for the averaging process. Other stress components for (e.g. vv^+ are obtained by exchanging the variables in Eq. (38) and (39). Figure 7 shows the Reynolds shear stress profiles for all the simulations.

The Musker law FPSV-WF showed reasonable agreement for $Re_\tau = 950$ and $2\,000$ for both grids. For the grid $N10$, the kink in the velocity profile at the second grid point was also visible in the Reynolds shear stress, having a larger value than in the DNS data. This affected all the rest of the profile, producing a larger slope of the curve than in the DNS data. The grid $N20$ shows a wide bump in the profile close to the wall for $Re_\tau = 2000$.

The D2V FPSV-WF shows large discrepancies in the profiles for $Re_\tau = 950$ and $2\,000$. The coarser grid $N10$ over predicted τ_w and u_τ, and the normalized Reynolds shear stress profiles displays smaller values and lower slopes than in the DNS data. With the grid $N20$ the situation improved, τ_w and u_τ decreased and the normalized Reynolds shear stress were closer to the reference, especially in the bulk of the domain. For the grid $N40$, the normalized Reynolds shear stress profiles for $Re_\tau = 2\,000$ and $16\,000$ were similar to those ones of grid $N20$. For $Re_\tau = 950$, the profile was similar to that one of grid $N20$ close to the wall and to that one of grid $N10$ at the centre of the channel.

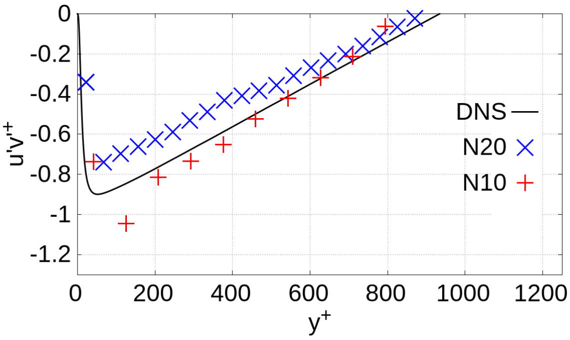

(a) $Re_\tau = 950$, Musker law

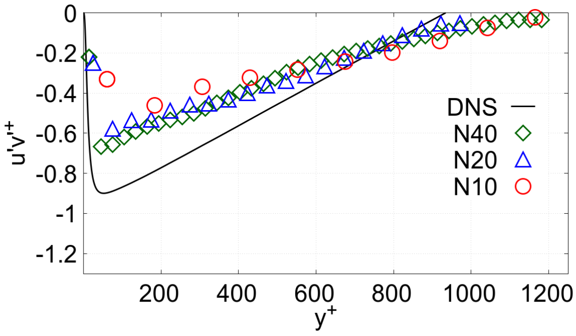

(b) $Re_\tau = 950$, D2V

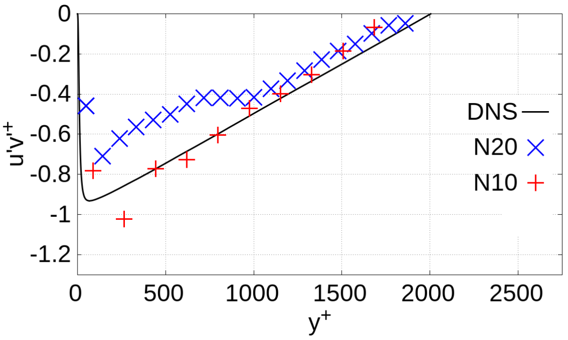

(c) $Re_\tau = 2\,000$, Musker law

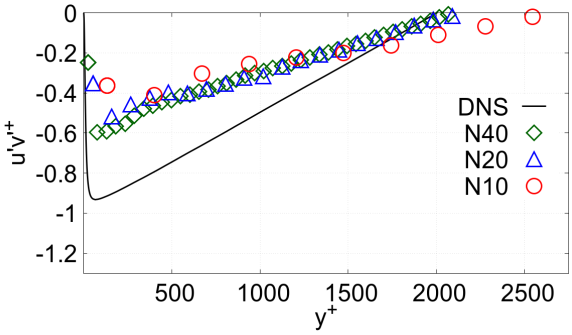

(d) $Re_\tau = 2\,000$, D2V

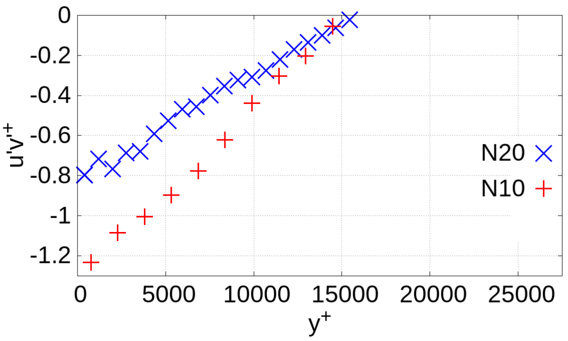

(e) $Re_\tau = 16\,000$, Musker law

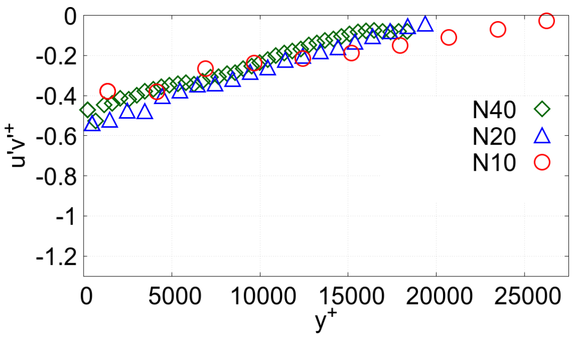

(f) $Re_\tau = 16\,000$, D2V

Figure 7: Reynolds shear stress for the three different grid resolutions N10, N20, N40, the three different frictional Reynolds numbers $Re_\tau = 950$ (a, b), $Re_\tau = 2\,000$ (c, d), $Re_\tau = 16\,000$ (e, f), and the two different FPSV-WF methods, Musker law (a, c, e) and D2V (b, d, f).

For the higher $Re_\tau = 16\,000$, no reference data were available for comparison. Nevertheless, their trends were in accordance with the profiles at lower Reynolds numbers for both the FPSV-WFs.

Figure 8 shows the Reynolds shear stress components $u'u'$, $v'v'$ and $w'w'$ obtained by the two methods for $Re_\tau = 2000$ compared to the DNS data from [34]. Here the D2V method gives results closer to the reference than the Musker law method. No improvement of the deviation from the reference is observed for higher resolution in the case of $u'u'$ and $v'v'$, especially for the Musker law.

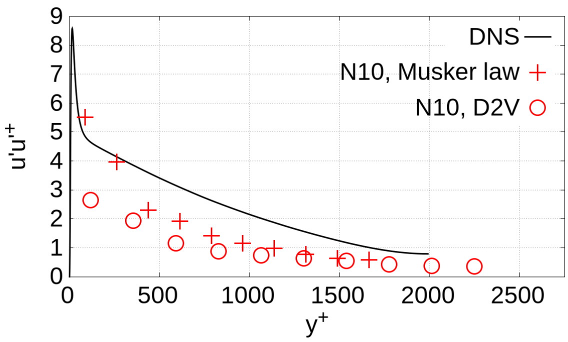

(a) $Re_\tau = 2\,000$, $N10$

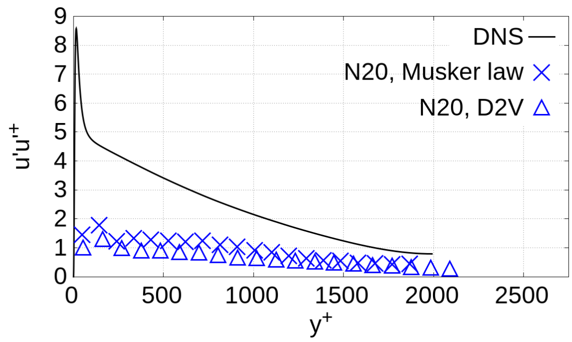

(b) $Re_\tau = 2\,000$, $N20$

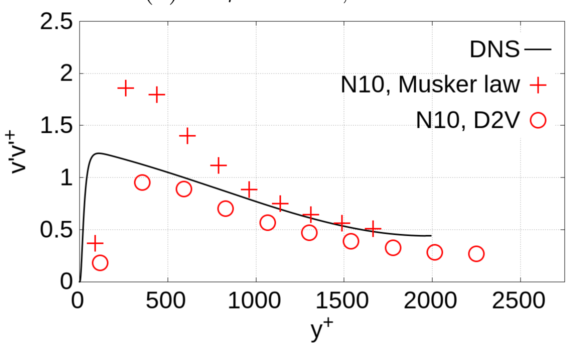

(c) $Re_\tau = 2\,000$, $N10$

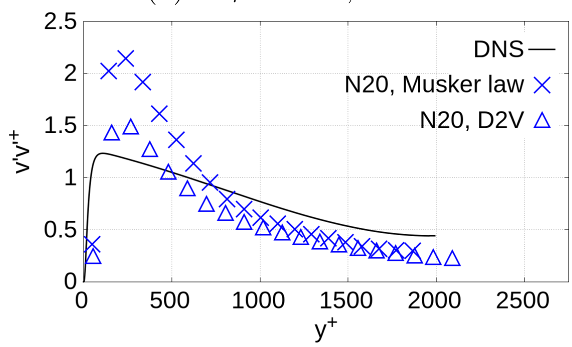

(d) $Re_\tau = 2\,000$, $N20$

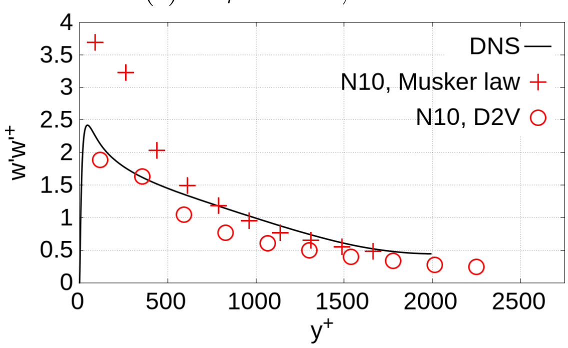

(e) $Re_\tau = 2\,000$, $N10$

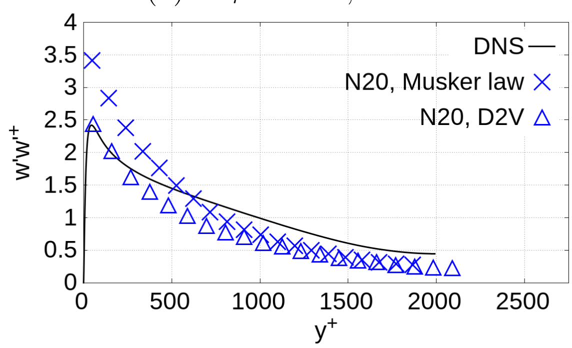

(f) $Re_\tau = 2\,000$, $N20$

Figure 8: Wall-normal Reynolds shear stress for $Re_\tau = 2\,000$ and two different resolutions compared to the DNS data from [34].

6 Conclusion and outlook

The FPSV-WF has been tested with turbulent channel flow simulations at different Reynolds numbers with very coarse grids. It is important to remark that under-resolved DNS (and also LES) will surely introduce numerical errors, and thus the wall function will not work as expected (over or under predictions) [32].

The Musker law FPSV-WF over predicted the normalized velocity and Reynolds shear stress profiles in the channel for all the Reynolds numbers tested (Figures 5a, 5c, 5e, 7a, 7c, and 7e). The reason could be due to the large kink at the second grid point, leading to the over estimation of the rest of the profile. While the velocity of the first grid point was enforced by the wall function, this does not hold for the second grid point. Therefore, the velocity at the second grid point depended on the grid resolution while at the first one it did not. The coarser grid $N10$ had a larger kink at the second grid node than the grid $N20$. The first grid point was also the boundary node where the wall function computed the wall shear stress applying the slip velocity. Therefore, the wall function did not depend on the grid resolution and both grids $N10$ and $N20$ gave results in a reasonable agreement with the DNS data. Because of the results for the grids $N10$ and $N20$ were already satisfactory, we did not perform simulations for the grid $N40$ with this method.

The D2V FPSV-WF showed discrepancies in all the profiles (Figures 5b, 5d, 5f, 7b, 7d, and 7f). The reason could be due to the method chosen for solving the second derivative of the velocity of Eq. (18) for obtaining the wall shear stress τ_w. The method computed a finite difference between the fluid node and the position of the wall. While this approach gave correct results of τ_w for the Poiseuille flow at low Reynolds number, it was strongly dependent on the grid resolution for turbulent flows at high Reynolds number. Especially for the coarser grid $N10$, τ_w was over estimated, leading to a lower slip velocity at the wall and to a lower position of the first grid point in the profiles in comparison to the reference data. By increasing the resolution with the grid $N20$, the error of the computed τ_w was lower, and all the profiles were in reasonable agreement with the DNS data, especially for the two lower $Re_\tau = 950$ and $2\,000$. For the higher $Re_\tau = 16\,000$ the error was still high. This was expected with respect to [32]. With under-resolved grids the information fed to the wall function from the first grid node presented errors which reduced the efficiency of the model. The finer grid $N40$ showed mixed results. For the lower $Re_\tau = 950$ the results were worse than for the grid $N20$, while for the other two Reynolds numbers were better. The reason can be that, for $Re_\tau = 950$, the y^+ of the first grid point was very close to the value of the intersection between the linear and the logarithmic profile of the "law of the wall" ($y^+ \approx 11$). This region is the zone where the transition from laminar to turbulent flow happens, which is a phenomenon very difficult to model. Nevertheless, the method proposed in Eq. (18) had the advantage to use information from cumulants, which was available directly at the boundary nodes.

The current work addressed an equilibrium turbulent boundary layer for a flat wall. Adverse pressure gradients where not considered.

Further work could be aimed at addressing the computation of the second derivative of the velocity by a more accurate method, e.g. by implementing Gauss-Legendre integration [19] or approximation methods [16]. For its application on curved geometries such as spheres or cars, the second derivative in wall normal direction of the velocity tangential to the wall can not be calculated with the cumulants of the D3Q27 lattice. The reason is that the cumulants of third order C_{300}, C_{030}, and C_{003} are missing. A new lattice that supports all ten third order cumulants definition can be used, e.g. the Body Centered Cubic (BCC) lattice [35] or the D3Q33 lattice.

Acknowledgments

This work is funded by the Technische Universität Braunschweig.

A Asymptotic analysis up to third order

Eq. (13) was derived after performing a combination of Taylor expansion [36] and asymptotic analysis [37] of equation Eq. (10) up to the third order in diffusive scaling [21], after rewriting it as [21]:

$$f_{ijkxyz(t+\Delta t)} = f^*_{ijk(x-ic\Delta t)(y-jc\Delta t)(z-kc\Delta t)t}. \tag{40}$$

The LHS of Eq. (40) can be Taylor expanded in time, the RHS can be Taylor expanded in space:

$$\sum_{o=0}^{\infty} \frac{\Delta t^o}{o!} \partial_{t^o} f_{ijkxyzt} = \sum_{m,n,l=0}^{\infty} \frac{(i^m j^n k^l)(-c\Delta t)^{m+n+l}}{m!n!l!} \partial_{x^m y^n z^l} f^*_{ijkxyzt}. \tag{41}$$

By inserting the moments $m_{\alpha\beta\gamma} = \sum_{ijk} i^\alpha j^\beta k^\gamma f_{ijk}$, it is possible to write:

$$\sum_{o=0}^{\infty} \frac{\Delta t^o}{o!} \partial_{t^o} m_{\alpha\beta\gamma} = \sum_{m,n,l=0}^{\infty} \frac{(-c\Delta t)^{m+n+l}}{m!n!l!} \partial_{x^m y^n z^l} m^*_{(\alpha+m)(\beta+n)(\gamma+l)}. \tag{42}$$

The expansion in moments can be used also with the cumulant collision operator since cumulants can be transformed into moments. Time and space variables are substituted by dimensionless ones by adopting diffusive scaling: $\Delta t \propto \epsilon^2$ and $\Delta x \propto \epsilon$, with $c\Delta t = \Delta x$. The term ϵ is the scaling parameter. Eq. (42) becomes:

$$\sum_{o=0}^{\infty} \frac{\epsilon^{2o}}{o!} \partial_{t^o} m_{\alpha\beta\gamma} = \sum_{m,n,l=0}^{\infty} \frac{(-\epsilon)^{m+n+l}}{m!n!l!} \partial_{x^m y^n z^l} m^*_{(\alpha+m)(\beta+n)(\gamma+l)}. \tag{43}$$

The moments are expanded asymptotically in ϵ:

$$m_{\alpha\beta\gamma} = \sum_{q=0}^{\infty} \epsilon^q m^{(q)}_{\alpha\beta\gamma}, \quad m^*_{\alpha\beta\gamma} = \sum_{q=0}^{\infty} \epsilon^q m^{*(q)}_{\alpha\beta\gamma}, \tag{44}$$

and Eq. (43) becomes:

$$\sum_{o=0}^{\infty} \frac{\epsilon^{2o}}{o!} \partial_{t^o} \sum_{q=0}^{\infty} \epsilon^q m^{(q)}_{\alpha\beta\gamma} = \sum_{m,n,l=0}^{\infty} \frac{(-\epsilon)^{m+n+l}}{m!n!l!} \partial_{x^m y^n z^l} \sum_{q=0}^{\infty} \epsilon^q m^{*(q)}_{(\alpha+m)(\beta+n)(\gamma+l)}. \tag{45}$$

Since the derivation is done for the D3Q27 lattice, only 27 moments are independent. The higher order moments are considered by aliasing condition:

$$m_{300} = m_{100}, \quad m_{400} = m_{200}, \quad m_{500} = m_{100}, \quad m_{310} = m_{110} \tag{46}$$

and so on. The moments are collision invariant at order zero ϵ^0 and first order ϵ^1 (no proof) [21]:

$$m^{(0)}_{\alpha\beta\gamma} = m^{*(0)}_{\alpha\beta\gamma}, \quad m^{(1)}_{\alpha\beta\gamma} = m^{*(1)}_{\alpha\beta\gamma} = m^{eq(1)}_{\alpha\beta\gamma}. \tag{47}$$

The relationship between the third order cumulants and the second derivative of the velocity is obtained at third order ϵ^3. For obtaining the second derivative in Y of the velocity in X ($\partial_{yy}u$), it is possible to write ($\alpha = 1$, $\beta = 2$, and $\gamma = 0$):

$$\begin{aligned} m^{(3)}_{120} + \partial_t m^{(1)}_{120} &= m^{*(3)}_{120} - \partial_x m^{*(2)}_{220} - \partial_y m^{*(2)}_{110} - \partial_z m^{*(2)}_{121} && (48)\\ &+{}^1\!/\!_2(\partial_{xx} m^{*(1)}_{120} + \partial_{yy} m^{*(1)}_{120} + \partial_{zz} m^{*(1)}_{122}) && (49)\\ &+\partial_{xy} m^{*(1)}_{210} + \partial_{xz} m^{*(1)}_{221} + \partial_{yz} m^{*(1)}_{111}. && (50) \end{aligned}$$

Due to Eq. (47), the moments of first order ϵ^1 can be written as ($\theta = {}^1\!/\!_3$ is the dimensionless speed of sound squared):

$$m^{*(1)}_{120} = \theta m^{(1)}_{100} = {}^1\!/\!_3 \rho^{(0)} u^{(1)}, \tag{51}$$

$$m^{*(1)}_{122} = \theta^2 m^{(1)}_{100} = {}^1\!/\!_9 \rho^{(0)} u^{(1)}, \tag{52}$$

$$m^{*(1)}_{210} = \theta m^{(1)}_{010} = {}^1\!/\!_3 \rho^{(0)} v^{(1)}, \tag{53}$$

$$m^{*(1)}_{221} = \theta^2 m^{(1)}_{001} = {}^1\!/\!_9 \rho^{(0)} w^{(1)}. \tag{54}$$

$$m^{*(1)}_{111} = 0, \tag{55}$$

The moment of second order $m^{*(2)}_{110}$ can be written as:

$$m^{*(2)}_{110} = (1 - \omega_1) m^{(2)}_{110} + \omega_1 m^{eq(2)}_{110}, \tag{56}$$

with $m^{(2)}_{110}$ [21]:

$$m^{(2)}_{110} = m^{*(2)}_{110} - (\partial_x m^{eq(1)}_{210} + \partial_y m^{eq(1)}_{120} + \partial_z m^{eq(1)}_{111}). \tag{57}$$

The following terms are introduced:

$$\begin{aligned} m_{110}^{eq(2)} &= \rho^{(0)} u^{(1)} v^{(1)}, && (58) \\ m_{210}^{eq(1)} &= \theta \rho^{(0)} v^{(1)} = {}^{1}\!/_{3} \rho^{(0)} v^{(1)}, && (59) \\ m_{120}^{eq(1)} &= \theta \rho^{(0)} u^{(1)} = {}^{1}\!/_{3} \rho^{(0)} u^{(1)}, && (60) \\ m_{111}^{eq(1)} &= 0. && (61) \end{aligned}$$

By inserting Eqs. (57) and (61) into Eq. (56), it is possible to write:

$$m_{110}^{*(2)} = \frac{(1-\omega_1)}{\omega_1} \left(-\partial_x {}^{1}\!/_{3} \rho^{(0)} v^{(1)} - \partial_y {}^{1}\!/_{3} \rho^{(0)} u^{(1)} \right) + \rho^{(0)} u^{(1)} v^{(1)}. \tag{62}$$

The moment of second order $m_{220}^{*(2)}$ can be written as:

$$m_{220}^{*(2)} = \theta \rho^{(0)} m_{200}^{*(2)} + \theta \rho^{(0)} m_{020}^{*(2)} - \theta^2 \rho^{(2)}, \tag{63}$$

where:

$$\begin{aligned} m_{200}^{*(2)} &= (1-\omega_1) m_{200}^{(2)} + \omega_1 m_{200}^{eq(2)}, && (64) \\ m_{020}^{*(2)} &= (1-\omega_1) m_{020}^{(2)} + \omega_1 m_{020}^{eq(2)}, && (65) \end{aligned}$$

and [21]:

$$\begin{aligned} m_{200}^{(2)} &= m_{200}^{*(2)} - (\partial_x m_{100}^{eq(1)} + \partial_y m_{210}^{eq(1)} + \partial_z m_{201}^{eq(1)}), && (66) \\ m_{020}^{(2)} &= m_{020}^{*(2)} - (\partial_x m_{120}^{eq(1)} + \partial_y m_{010}^{eq(1)} + \partial_z m_{021}^{eq(1)}), && (67) \end{aligned}$$

The following terms are introduced:

$$\begin{aligned} m_{200}^{eq(2)} &= \theta \rho^{(2)} + {u^{(1)}}^2 \rho^{(0)}, && (68) \\ m_{020}^{eq(2)} &= \theta \rho^{(2)} + {v^{(1)}}^2 \rho^{(0)}, && (69) \\ m_{100}^{eq(1)} &= \rho^{(0)} u^{(1)}, && (70) \end{aligned}$$

$$m_{201}^{eq(1)} = m_{021}^{eq(1)} = \theta\rho^{(0)}w^{(1)} = {}^{1}/{}_{3}\rho^{(0)}w^{(1)}, \tag{71}$$

$$m_{010}^{eq(1)} = \rho^{(0)}v^{(1)}. \tag{72}$$

451 By inserting Eqs. (72) into Eqs. (67), and Eqs. (67) into Eq. (A), it is possible to write:

$$m_{200}^{*(2)} = \theta\rho^{(2)} + u^{(1)^2}\rho^{(0)} - \tfrac{(1-\omega_1)}{\omega_1}(\partial_x\rho^{(0)}u^{(1)} + \partial_y 1/3\rho^{(0)}v^{(1)} + \partial_z 1/3\rho^{(0)}w^{(1)}), \tag{73}$$

$$m_{020}^{*(2)} = \theta\rho^{(2)} + v^{(1)^2}\rho^{(0)} - \tfrac{(1-\omega_1)}{\omega_1}(\partial_x 1/3\rho^{(0)}u^{(1)} + \partial_y\rho^{(0)}v^{(1)} + \partial_z 1/3\rho^{(0)}w^{(1)}). \tag{74}$$

452 By inserting Eqs. (74) into Eq. (63), the moment $m_{220}^{*(2)}$ becomes:

$$m_{220}^{*(2)} = 1/3\left(1/3\rho^{(2)} + u^{(1)^2}\rho^{(0)} - \tfrac{(1-\omega_1)}{\omega_1}(\partial_x\rho^{(0)}u^{(1)} + \partial_y 1/3\rho^{(0)}v^{(1)} + \partial_z 1/3\rho^{(0)}w^{(1)})\right) \tag{75}$$

$$+1/3\left(1/3\rho^{(2)} + v^{(1)^2}\rho^{(0)} - \tfrac{(1-\omega_1)}{\omega_1}(\partial_x 1/3\rho^{(0)}u^{(1)} + \partial_y\rho^{(0)}v^{(1)} + \partial_z 1/3\rho^{(0)}w^{(1)})\right) \tag{76}$$

$$-1/9\rho^{(2)}. \tag{77}$$

453 The moment of second order $m_{211}^{*(2)}$ can be written as:

$$m_{121}^{*(2)} = \theta m_{101}^{*(2)}. \tag{78}$$

454 The moment $m_{101}^{*(2)}$ can be derived similarly to the moment $m_{110}^{*(2)}$ in Eqs. (56)–(62). It
455 reads:

$$m_{101}^{*(2)} = \frac{(1-\omega_1)}{\omega_1}(-\partial_x 1/3\rho^{(0)}w^{(1)} - \partial_z 1/3\rho^{(0)}u^{(1)}) + \omega_1\rho^{(0)}u^{(1)}w^{(1)}. \tag{79}$$

456 The last step is to insert the Navier-Stokes momentum equation into the term $\partial_t m_{120}^{(1)}$:

$$\partial_t m_{120}^{(1)} = \partial_t\theta m_{100}^{(1)} = \partial_t 1/3\rho^{(0)}u^{(1)}. \tag{80}$$

457 The Navier-Stokes momentum equation for the X-component reads:

$$\partial_t u^{(1)} = -\partial_x u^{(1)^2} - \partial_y u^{(1)}v^{(1)} - \partial_z u^{(1)}w^{(1)} - \tfrac{1}{\rho^{(0)}}\partial_x p \tag{81}$$

$$+\tfrac{1}{3}\left(\tfrac{1}{\omega_1} - \tfrac{1}{2}\right)\left[\partial_{xx}u^{(1)} + \partial_{yy}u^{(1)} + \partial_{zz}u^{(1)}\right] + g_x. \tag{82}$$

Finally it is possible to rewrite Eq. (50) as:

$$m_{120}^{*(3)} - m_{120}^{(3)} = {}^{1}\!/_{3}\rho^{(0)}\partial_t u^{(1)} + \partial_x m_{220}^{*(2)} + \partial_y m_{110}^{*(2)} + \partial_z m_{121}^{*(2)} \tag{83}$$

$$-{}^{1}\!/_{2}(\partial_{xx} m_{120}^{*(1)} + \partial_{yy} m_{120}^{*(1)} + \partial_{zz} m_{122}^{*(1)}) \tag{84}$$

$$-\partial_{xy} m_{210}^{*(1)} - \partial_{xy} m_{221}^{*(1)} - \partial_{yz} m_{111}^{*(1)}. \tag{85}$$

The last step is to insert Eqs. (82), (79), (77), (62), (55), (54), (53), (52), and (51) into Eq. (85). By changing the moments with the cumulants, it is possible to obtain the relationship of Eq. (13):

$$C_{120}^{*} - C_{120} = -\frac{2}{9}\rho\left(\frac{1}{\omega_1} - \frac{1}{2}\right)[2\partial_{xy} v + \partial_{yy} u] + {}^{1}\!/_{3}\rho g_x + \mathcal{O}(\Delta x^2). \tag{86}$$

B Relaxation rates for the third order cumulants with limiter coefficient

The standard set of the relaxation rates for the third order cumulant is to put $\omega_3 = \omega_4 = \omega_5 = 1$. The collision reduces to $C^{*}_{\alpha+\beta+\gamma=3} = C^{eq}_{\alpha+\beta+\gamma=3} = 0$, i.e, the cumulants returns to equilibrium at every time step and the memory of the collision is erased. For this reason, the standard set shows superior stability properties, especially at high Re (low viscosities). However, discarding completely the memory of the collision we increase the leading error (numerical dissipation).

In order to reduce this error, a new set of relaxation rates has been introduced [22]. As shown in Eq. (29), they are related to the kinematic viscosity through the parameter ω_1. For high Re (low viscosities), $\omega_1 \to 2$ and thus $\omega_3 \to 0$, $\omega_4 \to 0$, $\omega_5 \to 0$, and $C^{*}_{\alpha+\beta+\gamma=3} \to C_{\alpha+\beta+\gamma=3}$. This means that the third order cumulants return very slowly to equilibrium, and they largely keep the memory of the collision. Hence for very low viscosities (high Re), in addition to a poor grid resolution, the simulation might become unstable.

For this reason we propose a limiter for the third order cumulants. The limiter avoids the third order cumulants growing excessively without affecting the reduced numerical dissipation. The idea is similar to the clipping method also used in some turbulence models [38] in order to limit the growth of certain variables which may otherwise increase indefinitely. Unlike in a classical clipping method our restriction is smooth. The bounded version of the new relaxation rates with limiter coefficient c_{lim} becomes [22]:

$$\omega_{3a}^{lim} = \omega_3 + \frac{(1-\omega_3)|C_{120}+C_{102}|}{|C_{120}+C_{102}| + \frac{c_{lim}}{\rho}}, \quad \omega_{3b}^{lim} = \omega_3 + \frac{(1-\omega_3)|C_{210}+C_{012}|}{|C_{210}+C_{012}| + \frac{c_{lim}}{\rho}}, \quad \omega_{3c}^{lim} = \omega_3 + \frac{(1-\omega_3)|C_{201}+C_{021}|}{|C_{201}+C_{021}| + \frac{c_{lim}}{\rho}}, \tag{87}$$

$$\omega_{4a}^{lim} = \omega_4 + \frac{(1-\omega_4)|C_{120}-C_{102}|}{|C_{120}-C_{102}| + \frac{c_{lim}}{\rho}}, \quad \omega_{4b}^{lim} = \omega_4 + \frac{(1-\omega_4)|C_{210}-C_{012}|}{|C_{210}-C_{012}| + \frac{c_{lim}}{\rho}}, \quad \omega_{4c}^{lim} = \omega_4 + \frac{(1-\omega_4)|C_{201}-C_{021}|}{|C_{201}-C_{021}| + \frac{c_{lim}}{\rho}}, \tag{88}$$

$$\omega_5^{lim} = \omega_5 + \frac{(1-\omega_5)|C_{111}|}{|C_{111}| + \frac{c_{lim}}{\rho}}, \tag{89}$$

where lim stands for bounded version with limiter coefficient. The collision of the third order cumulants becomes:

$$C_{120}^* + C_{102}^* = (1-\omega_{3a}^{lim})(C_{120}+C_{102}), \tag{90}$$

$$C_{210}^* + C_{012}^* = (1-\omega_{3b}^{lim})(C_{210}+C_{012}), \tag{91}$$

$$C_{201}^* + C_{021}^* = (1-\omega_{3c}^{lim})(C_{201}+C_{021}), \tag{92}$$

$$C_{120}^* - C_{102}^* = (1-\omega_{4a}^{lim})(C_{120}-C_{102}), \tag{93}$$

$$C_{210}^* - C_{012}^* = (1-\omega_{4b}^{lim})(C_{210}-C_{012}), \tag{94}$$

$$C_{201}^* - C_{021}^* = (1-\omega_{4c}^{lim})(C_{201}-C_{021}), \tag{95}$$

$$C_{111}^* = (1-\omega_5^{lim})C_{111}. \tag{96}$$

The limiter coefficient acts as follows:

- $\omega_{(\cdot)}^{lim} \to 1$ for $\rho|C_{(\cdot)}| \gg c_{lim}$, it restores the values of the rates to one (standard value),

- $\omega_{(\cdot)}^{lim} \to \omega_{(\cdot)}$ for $\rho|C_{(\cdot)}| \ll c_{lim}$, it sets the values of the rates to those ones calculated by Eq. (29).

For smooth solution the third order cumulants $C_{(\cdot)}$ do not deviate far from zero and the cumulant LBM uses the optimized relaxation rates. However, the third order cumulants may become large when the solution starts to oscillate, leading to unstable solutions. In this case, the c_{lim} acts to set the relaxation rates to the stable values (equal to one).

Table 3 reports the settings for the limiter coefficient c_{lim} for each simulation configuration. The parameters were selected manually close to the stability limit of the individual cases. The symbol (-) means a simulation with relaxation rates as in Eq. (29) without limiter coefficient. Interestingly, with only 20 grid nodes in the half channel eight ($N20$), the simulation at $Re_\tau = 950$ was performed without limiter coefficient. For the other simulations the value of c_{lim} was manually increased until a stable solution was obtained. Previous test have shown that the accuracy of the solution is only a weak function of c_{lim} such that its actual value was not very important. In the future, a more rigorous way of determing c_{lim} is desirable.

C Relaxation rates comparison

We compared simulation results based on the new set of the relaxation rates for the third order cumulants with the standard set equal to unity ($\omega_3 = \omega_4 = \omega_5 = 1$). The very coarse grid $N10$ together with the Musker law method for the FPSV-WF and the lower frictional Reynolds number $Re_\tau = 950$ was used. Due to the coarse resolution of the

Re_τ	$N10$	$N20$	$N40$
950	0.45	-	-
2 000	0.3	2.25	-
16 000	0.25	1	1

Table 3: Summary of the limiter coefficient c_{lim} for the turbulent channel flow simulations.

mesh, the simulation with the new set of the rates needed a limiter coefficient $c_{lim} = 0.45$ in order to obtain a stable solution, as reported in Table 3.

The instantaneous velocity colour plot on a slice at the centre of the channel showed large differences in the eddies size and turbulence intensity for the two sets of the relaxation parameters (Figure 9). With the standard set ($\omega_3 = \omega_4 = \omega_5 = 1$), the boundary layer did not become turbulent (Figure 9a). The new set produced an highly turbulent flows even with a very coarse grid (Figure 9b). The flow field in the bulk was greatly different, being smoother for the standard set and more turbulent for the new one.

The above results were confirmed by plotting the normalized velocity profiles and the normalized Reynold shear stress profiles in the direction normal to the planes (Figure 10). The standard set of the relaxation rates showed a lower y^+ at the first grid point and a higher velocity profile in comparison to the DNS data ($*$ points in Figure 10a). The new set showed a reasonable agreement with the DNS results ($+$ points in Figure 10a). The same observations held for the Reynold shear stress profiles. While the new set showed a good agreement with the DNS data ($+$ points in Figure 10b), the standard set gave considerably lower stresses close to wall ($*$ points in Figure 10b), thus confirming the lower turbulence intensity of this set of relaxation parameters.

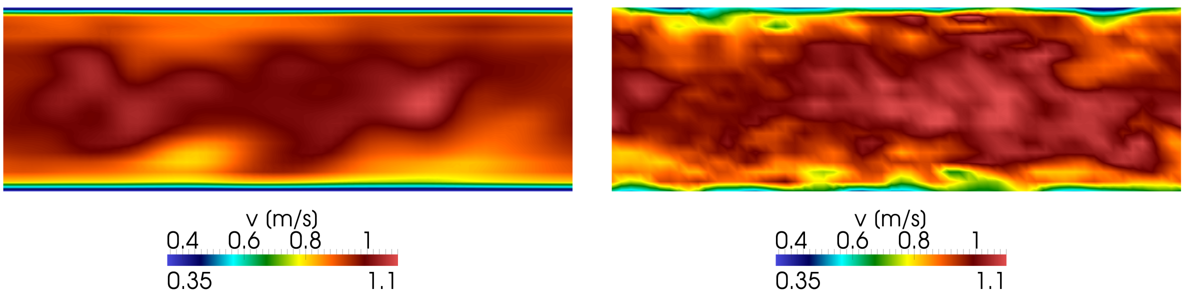

(a) Standard relaxation rates (b) New relaxation rates

Figure 9: Instantaneous velocity colour plot on a slice at the centre of the channel for the coarser resolution grid ($N10$) at $Re_\tau = 950$. Simulations were conducted with the Musker law FPSV-WF by using the relaxation rates equal to one (a) and new set of relaxation rates (b).

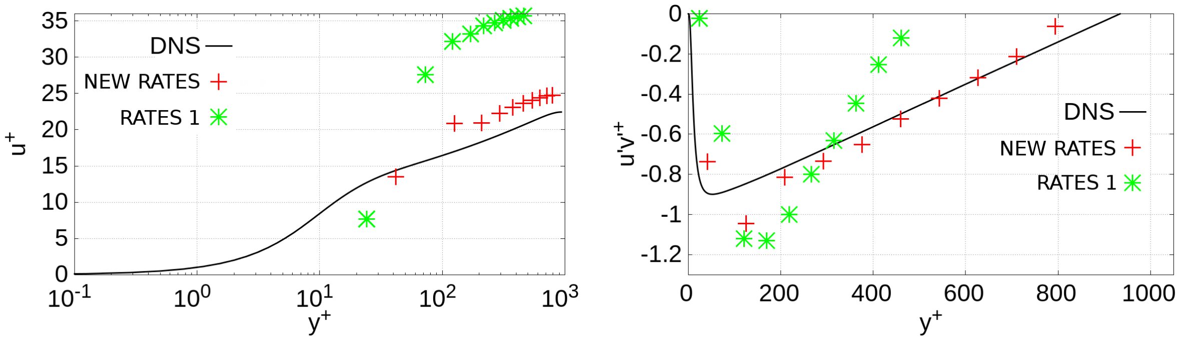

(a) Normalized velocity profile

(b) Reynolds shear stress

Figure 10: Normalized velocity profile (a) and Reynolds shear stress (b) for the coarser resolution grid ($N10$) at $Re_\tau = 950$. Simulations were conducted with the Musker law FPSV-WF by using the new set of the relaxation rates (NEW RATES) and the standard set equal to unity (RATES 1).

References

[1] H. Tennekes and J. L. Lumley. *A First Course In Turbulence*. MIT Press, 1972.

[2] S. Hoyas and J. Jiménez. Scaling of the velocity fluctuations in turbulent channels up to Reτ=2003. *Phys. Fluids*, 18(1):1–4, 2006.

[3] B.E. Launder and D.B. Spalding. The numerical computation of turbulent flows. *Comput. Methods Appl. Mech. Eng.*, 3(2):269–289, 1974.

[4] A. J. Musker. Explicit Expression for the Smooth Wall Velocity Distribution in a Turbulent Boundary Layer. *AIAA J.*, 17(6):655–657, 1979.

[5] P. A. Monkewitz, K. A. Chauhan, and H. M. Nagib. Self-consistent high-Reynolds-number asymptotics for zero-pressure-gradient turbulent boundary layers. *Phys. Fluids*, 19(11), 2007.

[6] T. Shih, L. A. Povinelli, N. Liu, M. G. Potapczuk, and J. L. Lumley. A Generalized Wall Function. *NASA*, 1999.

[7] T. Shih, L. A. Povinelli, N. Liu, and K. Chen. Generalized Complex Wall Function Turbulent for Flows. 2000.

[8] F. Tessicini, N. Li, and M. A. Leschziner. Simulation of Separation from Curved Surfaces with Combined LES and RANS Schemes. *Complex Effects in Large Eddy Simulations. Lecture Notes in Computational Science and Engineering*, 56, 2007.

[9] J. Hoffman. Simulation of turbulent flow past bluff bodies on coarse meshes using general galerkin methods: Drag crisis and turbulent euler solutions. *Comput. Mech.*, 38(4-5):390–402, 2006.

[10] N. Jansson and J. Hoffman. Computer simulation of incompressible flow past a circular cylinder at very high Reynolds numbers. 2011.

[11] E. Goraki, M. Geier, K. Kucher, and M. Krafczyk. Distributed cumulant lattice Boltzmann simulation of the dispersion process of ceramic agglomerates. *Jounal Comput. methods Sci. Eng.*, 16(2):231–252, 2016.

[12] E. Kian Far, M. Geier, K. Kutscher, and M. Krafczyk. Simulation of micro aggregate breakage in turbulent flows by the cumulant lattice Boltzmann method. *Computers and Fluids*, (140):222–231, 2016.

[13] A. Pasquali, M. Schönherr, M. Geier, and M. Krafczyk. Simulation of external aerodynamics of the DrivAer model with the LBM on GPGPUs. *Adv. Parallel Comput.*, 27:391 – 400, 2016.

[14] M. Weickert, G. Teike, O. Schmidt, and M. Sommerfeld. Investigation of the LES WALE turbulence model within the lattice Boltzmann framework. *Comput. Math. with Appl.*, 59(7):2200–2214, 2010.

[15] O. Malaspinas and P. Sagaut. Wall model for large-eddy simulation based on the lattice Boltzmann method. *J. Comput. Phys.*, 275:25–40, 2014.

[16] H. Schlichting. *Boundary-Layer Theory (Translated by J. Kestin).* McGraw-Hill Book Company, 1979.

[17] B.S. Baldwin and H. Lomax. Thin Layer Approximation and Algebraic Model for Separated Turbulent Flows. *AIAA 16th Aerosp. Sci. Meet.*, page 9, 1978.

[18] T. J. Craft. Numerical Solution of Boundary Layer Equations Example. *3rd Year Fluid Mech.*, 2008.

[19] S. Bocquet, P. Sagaut, and J. Jouhaud. A compressible wall model for large-eddy simulation with application to prediction of aerothermal quantities. *Phys. Fluids*, 24 (6), 2012.

[20] R. Benzi, S. Succi, and M. Vergassola. The lattice Boltzmann equation: theory and applications. *Phys. Rep.*, 222(3):145–197, 1992.

[21] M. Geier, M. Schönherr, A. Pasquali, and M. Krafczyk. The cumulant lattice Boltzmann equation in three dimensions: Theory and validation. *Comput. Math. with Appl.*, 70(4):507–547, 2015.

[22] A. Pasquali. *Enabling the cumulant lattice Boltzmann method for complex CFD engineering problems*. Ph.d. thesis, Technische Universität Braunschweig, 2017.

[23] D. D'Humières, I. Ginzburg, M. Krafczyk, P. Lallemand, and L. Luo. Multiple-relaxation-time lattice Boltzmann models in three dimensions. *Philos. Trans. A. Math. Phys. Eng. Sci.*, 360(1792):437–451, 2002.

[24] I. Ginzbourg and P. M. Adler. Boundary flow condition analysis for the 3-Dimensional lattice Boltzmann model. *J. Phys. II*, 4(2):191–214, 1994.

[25] I. Ginzburg and D. D'Humières. Multireflection boundary conditions for lattice Boltzmann models. *Phys. Rev. E. Stat. Nonlin. Soft Matter Phys.*, 68(6 Pt 2): 066614, 2003.

[26] M. Geier, M. Schönherr, A. Pasquali, and M. Krafczyk. Simulating the drag crisis behind a sphere with the lattice Boltzmann method: do or die. *13th Int. Conf. Mesoscopic Methods Eng. Sci.*, 2016.

[27] Martin Geier, Andrea Pasquali, and Martin Schönherr. Parametrization of the cumulant lattice boltzmann method for fourth order accurate diffusion part i: Derivation and validation. *Journal of Computational Physics*, 348:862–888, 2017.

[28] Martin Geier, Andrea Pasquali, and Martin Schönherr. Parametrization of the cumulant lattice boltzmann method for fourth order accurate diffusion part ii: Application to flow around a sphere at drag crisis. *Journal of Computational Physics*, 2017.

[29] A. Pasquali, M. Geier, and M. Krafczyk. LBMHexMesh: an OpenFOAM based grid generator for the Lattice Boltzmann Method (LBM). *7th Open Source CFD Int. Conf.*, 2013.

[30] C. Ybert, C. Barentin, C. Cottin-Bizonne, P. Joseph, and L. Bocquet. Achieving large slip with superhydrophobic surfaces: Scaling laws for generic geometries. *Phys. Fluids*, 19(12):17–19, 2007.

[31] X. Yang, Y. Mehmani, W. A. Perkins, A. Pasquali, M. Schönherr, K. Kim, M. Perego, M. L. Parks, N. Trask, M. T. Balhoff, et al. Intercomparison of 3d pore-scale flow and solute transport simulation methods. *Advances in Water Resources*, 95:176–189, 2016.

[32] J. Larsson and S. Kawai. Wall-modeling in large eddy simulation: length scales, grid resolution and accuracy. *Annual Research Briefs, Center for Turbulence Research*, 2010.

[33] O. Cabrit and F. Nicoud. Direct simulations for wall modeling of multicomponent reacting compressible turbulent flows. *Phys. Fluids*, 21(5), 2009.

[34] M. Lee and R. D. Moser. Direct numerical simulation of turbulent channel flow up to $Re_\tau \approx 5200$. *Journal of Fluid Mechanics*, 774:395–415, 2015.

[35] M. Namburi, S. Krithivasan, and S. Ansumali. Crystallographic Lattice Boltzmann Method. *Sci. Rep.*, 6(January):27172, 2016.

[36] F. Dubois. Equivalent partial differential equations of a lattice Boltzmann scheme. *Comput. Math. with Appl.*, 55(7):1441–1449, 2008.

[37] M. Junk, A. Klar, and L. Luo. Asymptotic analysis of the lattice Boltzmann equation. *J. Comput. Phys.*, 210(2):676–704, 2005.

[38] N. V. Kornev, I. V. Tkatchenko, and E. Hassel. A simple clipping procedure for the dynamic mixed model based on taylor series approximation. *International Journal for Numerical Methods in Biomedical Engineering*, 22(1):55–61, 2006.